The SOAR Gravitational Arc Survey – I. Survey overview and photometric catalogues[*]

Cristina Furlanetto,[1,2][†] Basílio X. Santiago,[1,2] Martín Makler,[2,3]
Eduardo S. Cypriano,[2,4] Gabriel B. Caminha,[2,3] Maria E. S. Pereira,[2,3]
Angelo Fausti Neto,[2] Juan Estrada,[5] Huan Lin,[5] Jiangang Hao,[5] Timothy A. McKay,[6]
Luiz N. da Costa[2,7] and Marcio A. G. Maia[2,7]

[1]*Departamento de Astronomia, Universidade Federal do Rio Grande do Sul, Av. Bento Gonçalves 9500, Porto Alegre, RS 91501-970, Brazil*
[2]*Laboratório Interinstitucional de e-Astronomia, Rua Gen. José Cristino 77, Rio de Janeiro, RJ 20921-400, Brazil*
[3]*Centro Brasileiro de Pesquisas Físicas, Rua Dr. Xavier Sigaud 150, Rio de Janeiro, RJ 22290-180, Brazil*
[4]*Instituto de Astronomia, Geofísica e Ciências Atmosféricas, Universidade de São Paulo, Rua do Matão 1226, São Paulo, SP 05508-090, Brazil*
[5]*Center for Particle Astrophysics, Fermi National Accelerator Laboratory, Batavia, IL 60510, USA*
[6]*Department of Physics, University of Michigan, 450 Church Street, Ann Arbor, MI 48109, USA*
[7]*Observatório Nacional, Rua Gen. José Cristino 77, Rio de Janeiro, RJ 20921-400, Brazil*

ABSTRACT

We present the first results of the SOAR (Southern Astrophysical Research) Gravitational Arc Survey (SOGRAS). The survey imaged 47 clusters in two redshift intervals centred at $z = 0.27$ and $z = 0.55$, targeting the richest clusters in each interval. Images were obtained in the g', r' and i' bands using the SOAR Optical Imager (SOI), with a median seeing of 0.83, 0.76 and 0.71 arcsec, respectively, in these filters. Most of the survey clusters are located within the Sloan Digital Sky Survey (SDSS) Stripe 82 region and all of them are in the SDSS footprint. Photometric calibration was therefore performed using SDSS stars located in our SOI fields. We reached for galaxies in all fields the detection limits of $g \sim 23.5$, $r \sim 23$ and $i \sim 22.5$ for a signal-to-noise ratio (S/N) = 3. As a byproduct of the image processing, we generated a source catalogue with 19 760 entries, the vast majority of which are galaxies, where we list their positions, magnitudes and shape parameters. We compared our galaxy shape measurements to those of local galaxies and concluded that they were not strongly affected by seeing. From the catalogue data, we are able to identify a red sequence of galaxies in most clusters in the lower z range. We found 16 gravitational arc candidates around eight clusters in our sample. They tend to be bluer than the central galaxies in the lensing cluster. A preliminary analysis indicates that ∼10 per cent of the clusters have arcs around them, with a possible indication of a larger efficiency associated with the high-z systems when compared to the low-z ones. Deeper follow-up images with Gemini strengthen the case for the strong lensing nature of the candidates found in this survey.

Key words: gravitational lensing: strong – surveys – galaxies: clusters: general.

1 INTRODUCTION

Tracing the evolution of galaxy cluster properties, in particular their mass distribution, has important implications for their use as cosmological probes, for understanding the nature of dark matter and dark energy, and to constrain galaxy evolution. A unique way to assess the mass distribution in clusters is through the arcs produced by strong gravitational lensing (Blandford & Narayan 1992; Hattori, Kneib & Makino 1999; Guzik & Seljak 2002; Mandelbaum et al. 2006; Treu 2010; Kneib & Natarajan 2012). In particular, the statistics of gravitational arcs may provide constraints on cosmological parameters and on scenarios of structure formation (Bartelmann et al. 1998, 2003; Golse, Kneib & Soucail 2002; Meneghetti et al. 2004; Kochanek et al. 2006; Hilbert, Metcalf & White 2007; Vuissoz et al. 2007; Zieser & Bartelmann 2012).

This motivated arc searches to be conducted, both in images from wide field surveys (Gladders et al. 2003; Cabanac et al. 2007; Estrada et al. 2007; Belokurov et al. 2009; Kubo et al. 2010; Kneib et al. 2010; Gilbank et al. 2011; Wen, Han & Jiang 2011; Bayliss 2012; More et al. 2012; Wiesner et al. 2012) and in fields targeting known clusters, with observations from the ground (Luppino et al. 1999; Zaritsky & Gonzalez 2003; Hennawi et al. 2008; Kausch et al. 2010) and from space (Sand et al. 2005; Smith et al. 2005; Horesh et al. 2010). Upcoming wide field imaging surveys, such as the Dark Energy Survey[1] (DES; Annis et al. 2005; The Dark Energy Survey Collaboration 2005), which started operations this year, are expected to detect about an order of magnitude more arcs than the current largest surveys.

For over a decade there has been a debate about the compatibility of the observed arc abundance with theoretical modelling. Bartelmann et al. (1998) suggested an apparent overabundance by approximately an order of magnitude of giant arcs on the sky as compared to Λcold dark matter (ΛCDM) predictions. Subsequent comparison works with limited statistics confirmed that the number of giant arcs on the sky is underpredicted by the ΛCDM cosmological model (Luppino et al. 1999; Gladders et al. 2003; Zaritsky & Gonzalez 2003; Li et al. 2006).

However, more recent studies including several factors that were not present in the first predictions, such as using simulations at the image level (Horesh et al. 2011; Boldrin et al. 2012) and including mergers (Redlich et al. 2012), have reduced the overall discrepancy between observed and predicted arc abundances (Dalal, Holder & Hennawi 2004; Horesh et al. 2005; Hennawi et al. 2007). In particular, Horesh et al. (2011) have carried out a study using simulations, where gravitational arcs are generated from ray-tracing of realistic sources from the *Hubble Ultra Deep Field* through clusters from the Millennium *N*-body simulation. The fraction of arcs per cluster in the simulated samples is compared to an arc sample in clusters with similar properties, using the same methods to identify the arcs in both samples. They find an overall consistency of the observed and simulated samples, at least in the redshift interval $0.3 < z < 0.6$. On the other hand, another comparison between arcs in X-ray selected clusters on data and on simulations (Meneghetti et al. 2011) still found a disagreement among them, although the discrepancy is smaller than the earlier estimates a decade ago. Also, including several baryonic effects on the simulations does not solve the remaining discrepancy (Killedar et al. 2012).

If on the one hand the arc statistics problem may have been solved or at least mitigated, issues remain regarding the variation of arc abundance with respect to the cluster redshift. For example, Gladders et al. (2003) found an overabundance of arcs in high-redshift clusters as compared to lower redshift ones. Gonzalez et al. (2012) found arcs in a cluster at $z = 1.75$, which should not be present at their image depths according to their modelling. Horesh et al. (2011) found an underprediction of clusters at $z \sim 0.2$ as compared to observations analysed in Horesh et al. (2005). These discrepancies could be due to the evolution of cluster structure with redshift (including the role of baryons) and/or to selection effects of the samples (e.g. X-ray versus optical selection). Caminha et al. (in preparation) model the variation of arc abundance with lens redshift stressing the effect of magnification on the expected distribution and finding an increase of arc incidence with z.

The main motivation for the *SOAR (Southern Astrophysical Research) Gravitational Arc Survey* (SOGRAS) was to constrain the variation of strong lensing efficiency as a function of cluster redshift, comparing the results with theoretical expectations. For this sake, we have designed a survey targeting clusters distributed in two redshift bins centred at $z \sim 0.3$ and $z \sim 0.5$. A total of 47 clusters were imaged in the g', r' and i' bands with the 4.1-m Southern Astrophysical Research Telescope (SOAR) from mid 2008 to early 2011.

The arcs and other strong lensing features found can be used to constrain the individual masses of the clusters (e.g. Cypriano et al. 2005). Another valuable information that can be drawn from the data is an estimate of ensemble cluster masses in each z bin with weak lensing, by stacking the profile of the scaled tangential distortion of background sources of all clusters in that bin. This technique has been applied successfully (Sheldon et al. 2001, 2004; Johnston et al. 2007) and leads to an averaged overall mass for the clusters.

Another motivation was to use this data set as a test bed for tools being developed for DES, in particular for gravitational arc studies, including testing automated arc-finders (using either morphology or colour) and methods to measure arc properties (e.g. Furlanetto et al. 2013). Indeed SOGRAS has comparable depth and seeing conditions as expected from DES and covers three of the five DES bands.

Finally, SOGRAS can be seen as a pathfinder for a high-resolution arc survey with SOAR using the recently commissioned SOAR Adaptive Module[2] (Tokovinin & Cantarutti 2008; Tokovinin et al. 2010).

In this paper we report on the overall properties of the survey, from the target selection and observations to data reduction and photometric calibration. We present the photometric catalogues, and discuss new gravitational arc candidates found by visual inspection. Detailed results on arc analyses and comparison with theoretical modelling will be presented in an accompanying paper.

As a by-product of the survey a large catalogue of galaxies in the cluster fields was generated, with astrometric, photometric and morphological information. This catalogue was used to separate cluster members (through the red sequence in the colour–magnitude diagrams) from field galaxies, and will be useful for future analysis of galaxy evolution.

The outline of this paper is as follows: Section 2 describes the survey, including information on sample selection, observational and image details. In Section 3 we describe the data reduction, including astrometric and photometric calibrations. We also carefully assess the quality of our photometry. The resulting galaxy catalogue is presented in Section 4. In the same section we present the first sample of arc candidates. Finally, in Section 5 we present our summary and closing remarks.

2 THE SURVEY

We have designed the survey to image a sample of galaxy clusters, equally split into two disconnected redshift bins, one at $0.20 < z_{phot} < 0.35$ (the 'low-z' bin) and the other at $0.50 < z_{phot} < 0.60$ (the 'high-z' bin), to have a 'leverage arm' to constrain the evolution of arc incidence between these two intervals.

The low-z bin was chosen such that there are enough reasonably rich clusters in this bin on the survey footprint (see Section 2.1) and to avoid having a too small arc probability. The high-z bin was determined by the availability of optical cluster catalogues

---

[1] www.http://www.darkenergysurvey.org/

[2] www.ctio.noao.edu/new/Telescopes/SOAR/Instruments/SAM/

in the survey footprint and by the requirement of having enough background sources to allow for a weak-lensing analysis by stacking the clusters in this bin (to have an overall estimate of the cluster masses).

All clusters were observed with the SOAR telescope, located on Cerro Pachón in the Chilean Andes, with the SOAR Optical Imager (SOI). The choice of telescope and instrument is motivated by the typical site seeing ($\simeq 0.8$ arcsec) and detector pixel size, which yield the required image quality for gravitational arc detection.[3]

The observations of all our targets were carried out in queue-scheduled mode assuring that our quality requirements were met. Therefore, this survey provides a fairly homogeneous sample, in the sense that all images were obtained in similar conditions, with the same instrument and filters and same exposure time, and is therefore well suited for a comparison of arc incidence.

The exposure time was determined by a balance between the number of clusters to be observed and the depth achieved for each cluster field for a given total observing time. Using the model for the number of arcs expected per cluster (as a function of limiting magnitude, cluster redshift, etc.) given in Caminha et al. (in preparation) and the exposure time calculator,[4] we found that the maximum total number of arcs is reached for integration times of about 10 min (in one single filter).

We also required to image in three bands such that colour information could be gathered, since this is an important information for discriminating gravitational arcs from cluster tidal features and for identifying multiple images. Furthermore, the colour information helps mitigating the contamination by foreground objects for weak-lensing mass reconstructions.

2.1 SDSS and Stripe 82

The baseline footprint for the targeting of our survey was the Sloan Digital Sky Survey (SDSS) 'Stripe 82', a 275 deg^2 equatorial stripe (over $-50 <$ RA < 59; $-1.25 <$ Dec. < 1.25), which was scanned multiple times in the fall seasons of 2000–2007 as part of a super-novae search, leading to a much deeper survey. The final Stripe 82 co-added data (hereafter *co-add*) reach $r \sim 23.5$ for galaxies, i.e. 2 mag fainter than the main SDSS (Annis et al. 2011).

The availability of these data allowed for the construction of deeper cluster catalogues, well suited for our target selection. In particular, red-sequence based cluster catalogues started to be produced as the first co-adds of several Stripe 82 visits were created. While single pass SDSS cluster catalogues reached up to $z \sim 0.3$ (Koester et al. 2007), catalogues obtained from the *co-add* reach $z \sim 0.6$, matching our requirement for the high-z bin, having at the same time some leverage arm with respect to the low-z bin and still allowing for a stacked weak-lensing measurement from our data.

At present, besides the deeper SDSS imaging, parts of Stripe 82 have been covered by a wealth of multi-wavelength data, such as the Large Area Survey (LAS) of the UKIRT Infrared Deep Sky Survey (UKIDSS) in the *YJHK* bands (Lawrence et al. 2007), deep *GALEX* UV imaging (Martin et al. 2005), the *Spitzer*-HETDEX Exploratory Large Area (SHELA) Survey (Papovich et al. 2011) and SpIES (Richards et al. 2012) surveys with *Spitzer*/IRAC, and the HeLMS (Oliver et al. 2012) and SPIRE (Cooray et al. 2010)

surveys with *Herschel*. At longer wavelengths, the whole Stripe lies within the footprint of Atacama Cosmology Telescope equatorial survey (Sehgal et al. 2012) and 80 deg^2 of the Stripe have deep VLA data (Hodge et al. 2011). Stripe 82 has also a very high density of spectroscopic redshifts, with redshift measurements from SDSS (Abazajian et al. 2009), 2dF (Colless et al. 2001; Croom et al. 2001), 2SLAQ (Croom, et al. 2009), 6dF (Jones et al. 2009), DEEP2 (Newman et al. 2012), VVDS (Garilli et al. 2008), PRIMUS (Coil et al. 2011), SDSS-III/BOSS (Ahn et al. 2012) and WiggleZ (Drinkwater et al 2010). This region is thus emerging as a 'deep extragalactic survey field', a precursor to DES and LSST, with an impressive array of multi-wavelength observations already in hand or in progress. SOGRAS may be used as a test case for combining the good imaging data from SOAR with this large set of complementary data, which strengthens the case to carry out most of our selection in this field.

In particular, during the second semester of 2010 until early 2011, 170 deg^2 of Stripe 82 were imaged in the i band for the CFHT/Megacam Stripe 82 Survey (CS82; Kneib et al. 2010; Erben et al., in preparation), providing data down to $i = 23.5$ obtained in excellent seeing conditions (median seeing of 0.6 arcsec), enabling precision weak-lensing measurements. This data set is particularly synergistic with SOGRAS. CS82 data will allow us to study the clusters imaged for SOGRAS at much larger radii and provide weak-lensing measurements for them. On the other hand the SO-GRAS data are useful for quality assessment on this new data set around clusters. For example, the star–galaxy separation and the determination of background and foreground sources can be tested in these fields thanks to the colour information at higher depths and better seeing than the SDSS photometric data.

2.2 Target selection and final galaxy cluster sample

The survey was carried out in two seasons: the first during semester 2008B and the second in 2010B (Makler et al. 2008, 2010). Since the cluster catalogues and status of the Stripe 82 co-add evolved during the two seasons, different catalogues were used for the selection. The procedure was nevertheless the same for both seasons: selecting the richest cluster catalogues in the same two redshift bins and requiring the same imaging conditions and instrument configurations. Therefore the two sets of observations are considered as a single data set.

The cluster selection for the 2008B season was carried out using a combination of three unpublished cluster catalogues on Stripe 82. The cluster finding methods were based on the red-sequence, accounting for its variation with redshift, and are precursors of the *Gaussian Mixture Brightest Cluster Galaxy* (GMBCG) cluster finder (Hao et al. 2010). However they differ in their likelihoods and the radial profiles used. All were run in the co-added data available in late 2006, providing an estimate of the cluster photometric redshift (z_{phot}) and richness.[5] We selected the richest clusters from these catalogues in the two redshift bins and ranked them by richness. The centres of the pointings were chosen as the cluster centre, defined as the position of the Brightest Cluster Galaxy (BCG) as determined by the cluster finding method.

We complemented this *main sample*, with an *extra sample* consisting of clusters detected on SDSS Data Release (DR) 6

---

[3] As is well known, the detectability of gravitational arcs is very sensitive to the point spread function (PSF) FWHM, because the seeing tends to decrease their length-to-width ratios and dilutes their surface brightness (e.g. Cypriano et al. 2001).

[4] http://www.noao.edu/gateway/ccdtime/

[5] Roughly the number of red-sequence galaxies in the cluster with luminosity above $L^\star/2$, where $L^\star$ is the characteristic luminosity in the Schechter (1976) luminosity function.
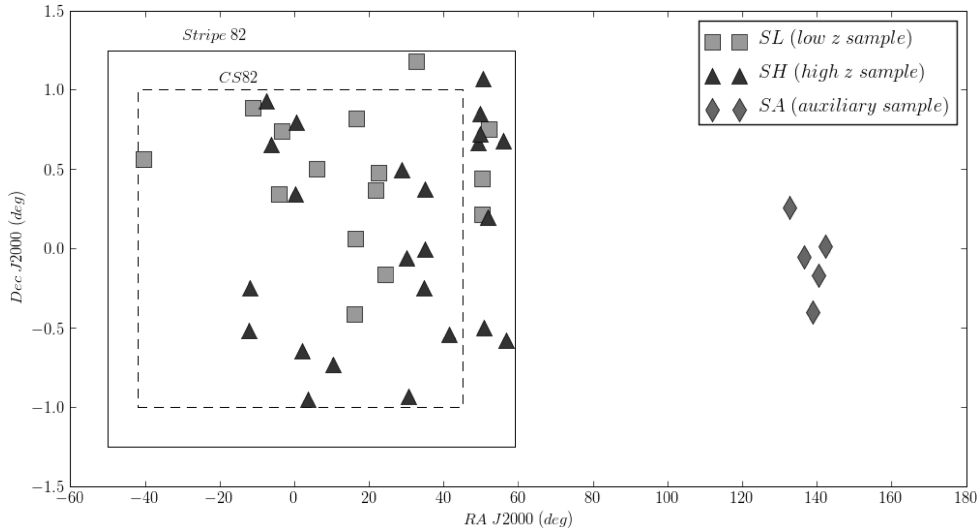
Figure 1. On-sky distribution of SOGRAS clusters. The area bounded by the dashed line is the CS82 footprint, which essentially is a subarea of the Stripe 82 footprint (bounded by the solid line). The auxiliary sample is outside of Stripe 82, but is still in the main SDSS footprint. For scale reasons, the three clusters of the extra sample whose positions are far from the equatorial stripe (SOGRAS0940+0744, SOGRAS1023+0413 and SOGRAS1054+1439) are not shown.

data (Adelman-McCarthy et al. 2008) – not necessarily on Stripe 82 – from the MaxBCG (Koester et al. 2007) catalogue that matched *ROSAT* X-ray sources and had good observability from SOAR on that semester. No redshift restriction was applied to this sample, which was chosen to improve our chances of finding arc systems and for scheduling flexibility (i.e. to allow observations to be made when observing conditions were not suitable for Stripe 82). Naturally, clusters observed from this sample are not suitable for our arc statistics purposes.

A visual inspection of SDSS single pass images using the Catalog Archive Server[6] (Takar et al. 2008; Abazajian et al. 2009) was made in order to avoid clusters close to bright stars, which could jeopardize the observations. We discarded all clusters that show diffraction spikes and star haloes within a $\sim$6.5 $\times$ 6.5 arcmin^2 field around the cluster centre. We also discarded fields with saturated stars within 3 arcmin from the cluster centre, imposing stronger limits on the magnitude closer to the centre (e.g. mag $\lesssim$ 14 for θ $\lesssim$ 1 arcmin). This eliminated $\sim$25 per cent of the selected fields. Clusters that appeared to have more than a single structure (e.g. could be line-of-sight superpositions) from this visual inspection were also avoided, eliminating $\sim$10 per cent of the selected clusters. While performing the visual inspection, we ignored any potential arc feature to avoid biasing the sample. The final result of this process was a set of two lists (one for each redshift bin) ordered by richness, containing a total of 60 selected clusters. The observers were told to select randomly among these lists, choosing the highest ranked object for which the observing conditions were favourable.

A total of 18 fields were observed in that season, 13 corresponding to clusters selected in the high-z bin, four in the low-z bin and one from the extra sample.

For the 2010B season we made a new selection of targets using the detections from a GMBCG cluster catalogue constructed using the complete *co-add* data (Annis et al. 2011). To exploit the synergy with CS82, only clusters in the footprint of this survey were selected. Again we selected the clusters on the two redshift bins and kept the richest ones. As in the 2008 sample, we also included an extra

sample with the same objects selected for that season. The visual selection procedure was the same as for the 2008 season.

Initially, 26 fields were observed, corresponding to 12 clusters detected in the high-z bin, 11 in the low-z bin and three from the extra sample.[7] At that point, the SOGRAS programme had still telescope time allocated, but the observability of Stripe 82 was unfavourable. Since there were more clusters observed from the high-z bin, than in the low-z one, clusters could be selected only in the later, thus requiring only shallower imaging. Therefore an *auxiliary sample* was chosen, following the same selection criteria as the low-z one, but choosing clusters at higher *RA* in an equatorial region covered by SDSS single pass imaging. These clusters were taken from a GMBCG catalogue based on SDSS DR7 data (Hao et al. 2010). Seven fields from this sample were observed, completing the survey. Two of these had large overlaps on their central regions with other pointings on the same sample. Therefore we consider the auxiliary sample as composed by only five independent fields.

Thus a total of 47 independent cluster fields were observed for this project with SOAR (accounting for the overlapping fields in the sample).

The on-sky distribution of the observed fields is shown in Fig. 1. From the 47 observed clusters, 39 are in the main sample, five are in the auxiliary 2010 sample and three are in the extra sample. For arc statistics analysis, the auxiliary sample can be added to the main sample, since its clusters were selected following the same criteria for redshift and richness. Although the clusters in the auxiliary sample were taken from a shallower photometric catalogue, the same cluster finder algorithm (GMBCG) was used to generate the cluster catalogue in the main SDSS area and in the *co-add* and it is known to be complete for the low-z clusters. The resulting split

---

[6] http://cas.sdss.org/dr6/en/tools/chart/list.asp

[7] Two fields had a large overlap with pointings from the 2008B season. Since the possible arc candidates will be located close to the cluster centre, we considered those fields as a single one. In this case we kept only the 2010B fields in our imaging sample, due to both the better quality of the imaging and the improved determination of cluster properties from the catalogue used for this selection. This improved cluster detection made the object observed as part of the extra sample in 2008B to correspond to a pointing in the low-z sample.
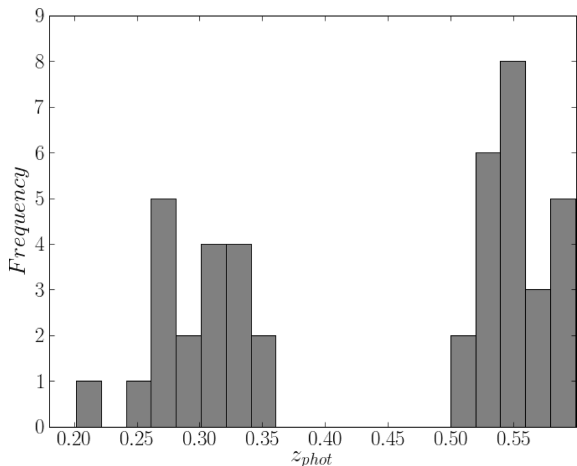
Figure 2. Distribution of main sample clusters as a function of photometric redshift.

in z was 24 clusters in the high-z bin and 20 in the low-z bin. The three clusters in the extra sample cannot be included in a statistical analysis because they were selected following other criteria. The distribution of photometric redshifts for the SOGRAS clusters is shown in Fig. 2.

A summary of the properties of the SOGRAS clusters is given in Table 1. The mean photo-z (fourth column) uncertainty is 0.03 (Reis et al. 2012). The fifth column, N_{gals}^i, shows the richness as taken from the original selection catalogues. As mentioned above, these catalogues were obtained from different methods (three for 2008B, one for 2010B) and different data (different number of co-adds for 2008B and 2010B, plus the single pass data for the Auxiliary Sample). Therefore, those richnesses cannot be compared directly. To provide a more uniform estimate of the richness, we have run a single code, the Error Corrected Gaussian Mixture Model (ECGMM; Hao et al. 2010), over all observed fields on the final Stripe 82 co-add data, providing a new richness estimate for these clusters (sixth column, $N_{\mathrm{gals}}^{\mathrm{GM}}$). We used the run on the DR7 data (Hao et al. 2010) to provide a richness for the objects outside Stripe 82. However, as the single pass and co-add data have different signal-to-noise ratio (S/N), again the richness cannot be compared. Using the richness from both the single pass, $N_{\mathrm{gals}}^{\mathrm{DR7}}$, and co-add data, $N_{\mathrm{gals}}^{\mathrm{co\text{-}add}}$, for clusters on Stripe 82 we obtained a mean relation connecting them: $N_{\mathrm{gals}}^{\mathrm{co\text{-}add}} = 0.40 \times N_{\mathrm{gals}}^{\mathrm{DR7}} + 12.3$. Applying this relation to the objects on our sample outside Stripe 82 we obtain a 'renormalized' richness estimate[8] that should be more comparable among all clusters in the sample ($N_{\mathrm{gals}}^{\mathrm{GM}}$).

2.3 Observations

Observations of all our targets were carried out with SOI, which consists of a mini-mosaic of two E2V CCDs, each one with 4096×2048 pixels, covering a field of view of 5.25×5.25 arcmin^2. A 2×2 binning was used, yielding a detector scale of 0.154 arcsec pixel^{-1}. The exposures were taken in fast read-out mode. Bias and flat-field images were also observed on the same nights, except for the nights 2008-10-03 and 2008-11-21.

---

[8] These values should be interpreted with care, since it is well known that the richness from optical clusters has a very large scatter and the relation above is only a mean relation.

Each target field in our programme was imaged in the g', r' and i' filters. For each filter we had three exposures of 180 s, which were slightly dithered by $\sim$10 arcsec in the direction perpendicular to the gap between the SOI CCDs. This dithering pattern allowed us to fill the gap region as well as to remove CCD defects and cosmic ray hits. The centre of the target cluster was placed at 30 arcsec from the gap to the east direction.

To achieve the image quality needed for the survey in order to increase the arc detection efficiency, we required a seeing full width at half-maximum (FWHM) smaller than 0.8 arcsec. We also required an airmass constraint of $X \leq 1.5$, which is adequate for targets close to the celestial equator imaged from SOAR. Finally, we required nights with $\leq$7 d from New Moon, to reduce the noise over the images, mainly in the g' band.

3 DATA REDUCTION

The individual exposures of each SOGRAS field were bias-subtracted and flat-fielded using standard tasks from the MSCRED package of the Image Reduction and Analysis Facility (IRAF). For the nights in which there were no bias and flat-field exposures, exposures of the previous night were used.

Custom codes were employed to remove the fringe pattern from i'-band images, since the defringing performed by IRAF MSCRED tasks was not satisfactory and we found that it could be improved upon. Our codes identify pixels on top of the fringing pattern and compute median counts for them, both for the sky-subtracted science and fringing correction images, computing the ratio between the two. They then scale the correction frame by this ratio before subtracting the pattern from the science image. The fringe amplitude (i.e. the typical difference between peak and valley in the fringe pattern) in the raw data was approximately four per cent of the sky and was reduced to levels smaller than 1 per cent of the sky by our defringing method for most of our i'-band images. However, we noticed a remaining fringing residual, especially in the west CCD chip, for about 12 per cent of our i'-band images. This residual fringing amplitude was at worst $\sim$2 per cent of the sky level. We also noticed a small difference in the counts of the four SOI amplifiers ($<$2 per cent) and a difference in the noise level between the two CCDs.

The original Multiple Extension Format (MEF) files were then converted into Flexible Image Transport System (FITS) files using the task SOIMOSAIC from the SOAR/SOI IRAF package.

Exposures of the same filter of each target were aligned and combined into a stacked image, by taking the median at each position. This stacked image was used for object detection and photometry. The stacked images in each filter were aligned with the task WREGISTER from IRAF, using the i'-band image as reference. We also combined the g', r' and i' stacked images of each cluster to have a final $g' + r' + i'$ co-added image, using IRAF's task IMCOMBINE (each image was scaled by the mean before being added). This co-added image was used to visually inspect for gravitational arc candidates.

We measured the seeing in the stacked images for each band using the IMEXAMINE IRAF task. The distribution is shown in Fig. 3. Clearly most of the images do satisfy our seeing constraint, at least in the i' band, and are therefore well suited for finding arcs. Only two clusters have seeing larger than 1 arcsec in that band. They were observed in windy conditions and their images have relatively poor seeing. The median seeing for all images is 0.83 arcsec, 0.76 arcsec and 0.71 arcsec in the g', r' and i' bands, respectively.

Table 1. Summary of the SOGRAS galaxy cluster sample.

Cluster ID	RA (J2000)	Dec. (J2000)	z_{phot}	N^i_{gals} a	N^{GM}_{gals} b	Observation date
SOGRAS0001+0020	00:01:01	00:20:17	0.538	39	6	2008-11-20
SOGRAS0001+0047	00:01:56	00:47:21	0.527	37	6	2008-10-03
SOGRAS0008−0038	00:08:21	−00:38:45	0.523	32	53	2010-12-02
SOGRAS0014−0057	00:14:54	−00:57:08	0.535	62	46	2010-10-31
SOGRAS0024+0030	00:24:00	00:30:07	0.292	33	30	2010-11-01
SOGRAS0041−0043	00:41:09	−00:43:49	0.564	28	26	2010-12-02
SOGRAS0104−0024	01:04:24	−00:24:51	0.266	26	24	2010-12-08
SOGRAS0104+0003	01:04:55	00:03:36	0.272	85	66	2010-10-31
SOGRAS0106+0049	01:06:07	00:49:10	0.263	35	32	2010-10-31
SOGRAS0127+0022	01:27:13	00:22:06	0.338	26	40	2010-11-01
SOGRAS0130+0028	01:30:36	00:28:39	0.335	24	27	2010-12-08
SOGRAS0137−0009	01:37:29	−00:09:56	0.341	37	38	2010-10-31
SOGRAS0155+0029	01:55:38	00:29:42	0.525	36	9	2008-11-20
SOGRAS0200−0003	02:00:33	−00:03:46	0.580	41	47	2010-10-31
SOGRAS0202−0055	02:02:23	−00:55:57	0.599	43	34	2010-10-31
SOGRAS0210+0110	02:10:56	01:10:44	0.276	88	35	2008-11-21
SOGRAS0218−0014	02:18:45	−00:14:52	0.502	34	73	2010-11-01
SOGRAS0219+0022	02:19:49	00:22:25	0.531	36	35	2008-10-03
SOGRAS0220−0000	02:20:03	−00:00:18	0.555	28	42	2010-12-08
SOGRAS0245−0032	02:45:27	−00:32:36	0.580	54	42	2010-10-31
SOGRAS0316+0039	03:16:46	00:39:54	0.554	31	7	2008-11-20
SOGRAS0319+0042	03:19:25	00:42:52	0.546	32	4	2008-11-04
SOGRAS0319+0050	03:19:44	00:50:55	0.576	40	23	2008-11-20
SOGRAS0320+0012	03:20:47	00:12:43	0.255	24	9	2008-11-21
SOGRAS0321+0026	03:21:11	00:26:20	0.309	47	34	2008-11-21
SOGRAS0321+0103	03:21:57	01:03:59	0.549	31	2	2008-11-04
SOGRAS0322−0030	03:22:56	−00:30:06	0.543	41	30	2008-11-21
SOGRAS0327+0011	03:27:09	00:11:32	0.549	31	27	2009-01-02
SOGRAS0328+0044	03:28:15	00:44:51	0.322	41	30	2009-01-02
SOGRAS0343+0041	03:43:57	00:41:31	0.511	33	0	2008-11-04
SOGRAS0346−0035	03:46:39	−00:35:03	0.541	31	10	2009-01-02
SOGRAS0850+0015[c, d]	08:50:23	00:15:36	0.202	42	29	2011-01-11
SOGRAS0905−0003[c]	09:05:52	−00:03:19	0.305	30	24	2011-01-12
SOGRAS0916−0024[c, d]	09:16:09	−00:24:16	0.345	78	43	2011-01-11
SOGRAS0921−0010[c]	09:21:41	−00:10:18	0.305	35	26	2011-01-12
SOGRAS0928+0000[c]	09:28:45	00:00:55	0.307	47	31	2011-01-12
SOGRAS0940+0744[e]	09:40:53	07:44:25	0.390	68	39	2011-01-11
SOGRAS1023+0413[e]	10:23:39	04:13:08	0.465	42	29	2011-01-11
SOGRAS1054+1439[e]	10:54:17	14:39:04	0.328	118	59	2011-01-12
SOGRAS2118+0033	21:18:49	00:33:37	0.276	68	53	2010-10-31
SOGRAS2311−0030	23:11:06	−00:30:59	0.594	34	39	2010-11-01
SOGRAS2312−0015	23:12:52	−00:15:02	0.588	51	40	2010-10-03
SOGRAS2315+0053	23:15:45	00:53:12	0.326	32	37	2010-11-01
SOGRAS2330+0055	23:30:09	00:55:51	0.548	40	40	2010-11-01
SOGRAS2335+0039[d]	23:35:42	00:39:20	0.564	46	23	2010-11-01
SOGRAS2343+0020[d]	23:43:34	00:20:37	0.269	55	37	2010-10-31
SOGRAS2346+0044	23:46:30	00:44:23	0.291	37	28	2010-11-01

[a]Richness taken from the original selection catalogues.
[b]Richness obtained with the ECGMM method on the final Stripe-82 co-added data. In the case of clusters from the auxiliary data, this value is converted from the single pass data as described in the text.
[c]Cluster from the auxiliary sample.
[d]These fields have overlapping observations.
[e]Cluster from the extra sample.

3.1 Astrometric calibration

For the construction of the world coordinate system (WCS) of each stacked image, we used The Guide Star Catalog, Version 2.3.2, GSC2.3-STSCI (Lasker et al. 2008) and pattern matched the positions of the stars against those in the SOGRAS fields, producing a list with the RA, Dec. and Cartesian (x and y) coordinates of the selected stars. For this process we selected a subsample of the brightest (but not heavily saturated) stars yielding typically about 20 stars for each SOGRAS field. The residuals in the astrometric
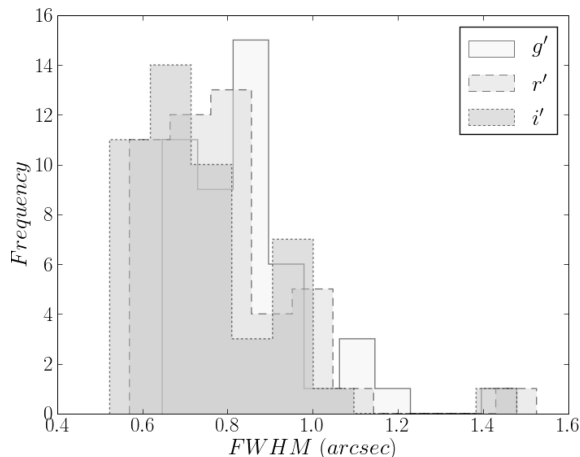
Figure 3. Seeing FWHM distribution of the SOGRAS fields.

solutions for RA and Dec. are of the order of 0.15 arcsec, which is sufficient to enable a proper positional matching to SDSS for the photometric calibration.

3.2 Photometric calibration

We used public SDSS data to calibrate the photometry of our stacked images. Following the standard SDSS system, we hereafter refer to our calibrated data as g, r and i magnitudes. Most fields we observed belong to the SDSS Stripe 82 and therefore have easily available and very accurate photometric calibrations (Ivezić et al. 2007).

The technique we employed to calibrate our sample was as follows. The first step was to select bright but unsaturated stars from SDSS DR7 (Ivezić et al. 2007) in the SOGRAS fields. For each field, we detected objects with SEXTRACTOR Version 2.8.6 (Bertin & Arnouts 1996) and defined as stars objects whose star–galaxy classification parameter CLASS_STAR, as measured by SEXTRACTOR in the i-band image, was larger than 0.85. Those were matched to the stars in the SDSS catalogue, yielding typically about 10 stars per SOGRAS field. Then we computed the mean offset between the magnitudes measured with SEXTRACTOR's automatic aperture (MAG_AUTO) and their corresponding SDSS magnitudes (MODEL_MAG), and used this offset as the zero-point of the magnitude scale of each filter for that field. The mean (dispersion) values are 31.46 (0.15), 31.35 (0.10) and 30.90 (0.10) for g, r and i filters, respectively.

Given the lack of actual photometric standards in our calibration process and the fact that our focus is on extended objects, we refrained from adopting colour terms in the calibration, whose amplitude is likely smaller than the uncertainties in the galaxy photometry.

3.3 Galaxy photometry

We used SEXTRACTOR to identify sources and measure their magnitudes. Based on provided detection thresholds, SEXTRACTOR determines the background around each source and whether a given pixel belongs to the source or to the background. SEXTRACTOR automatic aperture photometry (MAG_AUTO) was adopted in this work. It is based on flexible elliptical apertures around every detected object and is intended to give a precise estimate of total magnitudes, at least for galaxies.

An automated pipeline in python was created to expedite the process of object finding, photometry (including application of photometric calibration described earlier) and catalogue construction. This pipeline uses functions from SLTOOLS,[9] a library for image processing, catalogue manipulation and strong lensing applications (Brandt et al., in preparation). In the following we provide a brief description of this pipeline.

For each SOGRAS field, our pipeline runs SEXTRACTOR separately for the g, r and i stacked images, using the previously determined zero-points. Sources with more than 10 contiguous pixels and whose flux exceeds 2σ above the sky background were considered as real detections.[10] Therefore, the resulting AUTO magnitudes for the same galaxy in different filters are meant to quantify their total fluxes. We did experience with flux measurements in the same aperture and area, using SEXTRACTOR in the dual image mode, taking the i-band image as reference image (i.e. using the aperture defined in i-band image for measuring magnitudes on the images taken in g and r), but this procedure resulted in systematics in colours 10–50 per cent larger than those presented here (see the next section).

In Section 4 we describe the resulting catalogues in more detail.

3.4 Photometric quality assessment

In order to assess the quality of the SOGRAS photometry, we again used the well-calibrated data from SDSS, given the overlap of the SOGRAS fields with the SDSS footprint. We began by performing an object matching for each SOGRAS field, as was done in the selection of stars for photometric calibration.

We compare our magnitudes and colours to those from SDSS in order to assess our photometric errors and their dependence on S/N level. In Fig. 4 we show, as an example, the comparison of i-band magnitudes and $(r - i)$ colours for both stars (shown on the left-hand panels) and galaxies (right-hand panels) in the field of the cluster SOGRAS0850+0015. At the bright end, the scatter in the plots is dominated by the differences in the way magnitudes were measured in SOGRAS and SDSS, and by the residuals in photometric calibration. On the other hand, at the faint end of the plots, the larger scatter is probably caused by the low S/N levels of these objects, especially in SDSS, which is shallower than SOGRAS. No significant systematics is seen in the stellar photometry, indicating that the photometric calibration is effective. After applying a 2.5σ clipping to eliminate outliers, we find a mean offset of $\langle i - i_{\mathrm{SDSS}} \rangle = 0.02$ for $i < 19$. The *rms* SOGRAS–SDSS residual is $i = 0.04$ in the same range. Stellar colours have slightly larger systematic residuals $(r - i) - (r - i)_{\mathrm{SDSS}} = 0.05$ with an *rms* value of 0.04 when bright stars are considered. These values are typical of the other fields.

As for the galaxies, the mean offsets in i magnitudes and $(r - i)$ colours depicted in Fig. 4 are comparable to those of stars. But the scatter is larger as can be attested from a visual inspection of Fig. 4. This reflects the difficulty in measuring their total fluxes, specially for faint objects, and also the differences in the SOGRAS and SDSS PSFs. The *rms* residuals are 0.06 both for magnitudes and for colours. The scatter plot in colours also reveals a systematic trend of SOGRAS galaxies being redder (bluer) for blue (red) colours, which is another way of concluding that the SOGRAS colour distributions are narrower than those from SDSS. This is just as expected

---

[9] The SLTOOLS library is available at http://che.cbpf.br/sltools/
[10] The remaining parameters used for object detection and catalogue generation with SEXTRACTOR can be obtained from the configuration file, which is available upon request to the corresponding author.
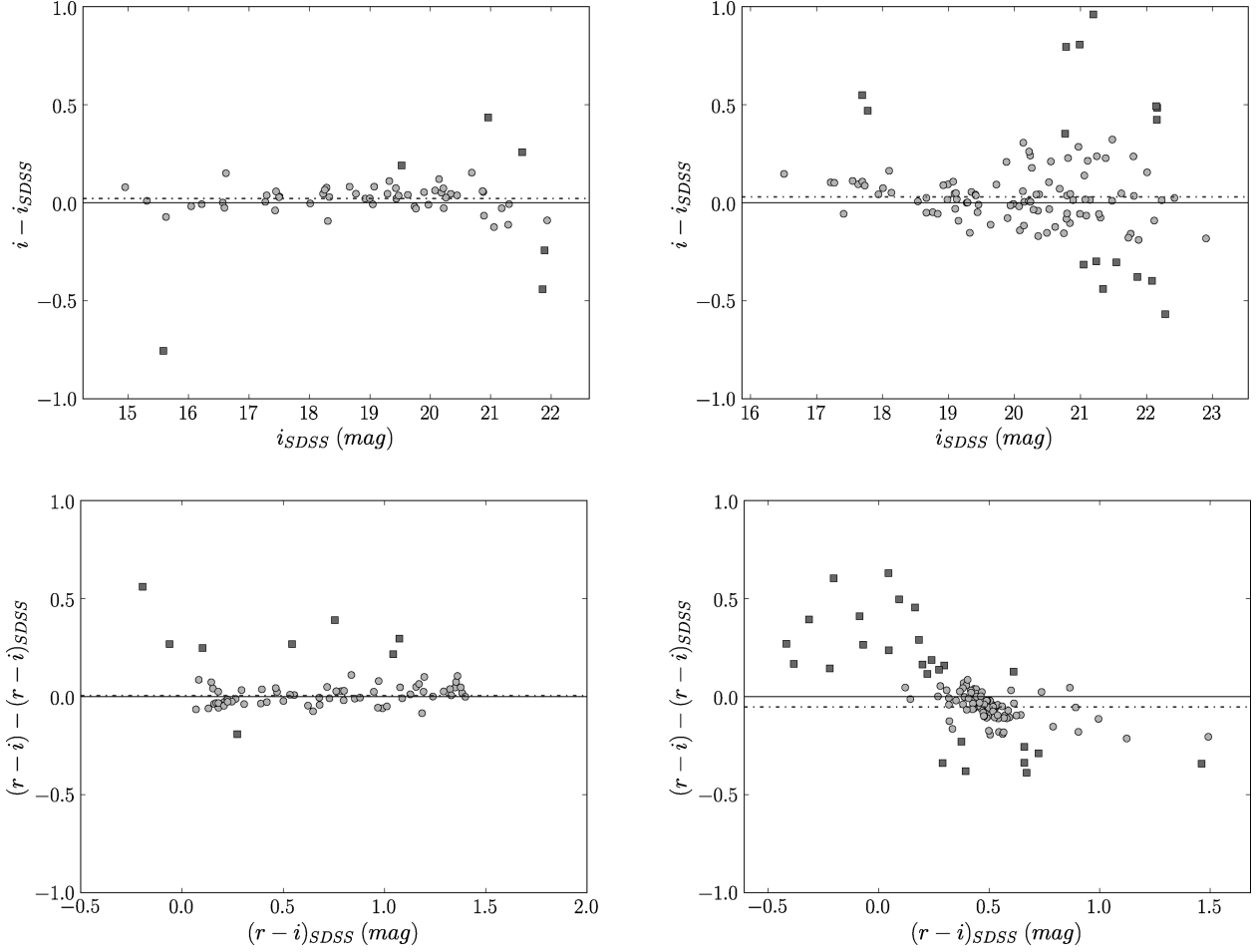
Figure 4. Differences in *i*-band magnitude (upper panels) and $(r - i)$ colour (lower panels) between SOGRAS and SDSS for both stars (left-hand panels) and galaxies (right-hand panels) in the field around the cluster SOGRAS0850+0015. Only objects with $r < 22.5$ were used in the plots. The solid line corresponds to zero residual. The square points were 2.5σ clipped out before computing the mean residual (dashed line).

from the higher photometric precision and image quality from our SOAR data.

We now extend our photometric quality assessment to the other SOGRAS fields. In Fig. 5, the panels on the left show the distribution, over all fields, of the mean difference between our magnitudes and those from SDSS using bright sources only. The panels on the right show the *rms* difference, computed as follows:

$$\text{rms} = \frac{1}{\sqrt{2}} \left(\frac{\sum_{j=1}^{N} (m_j - m_{j,\text{SDSS}})^2}{N} \right)^{1/2}, \tag{1}$$

where m_j are the individual magnitude measurements from either surveys in a given field and N is the number of bright sources in that field. By *bright sources* in this figure we mean those with $g < 20$, $r < 20$, $i < 19$. The $\sqrt{2}$ factor in the expression for the *rms* accounts for the fact that errors in *both* SDSS and SOGRAS contribute in quadrature to this statistic. Therefore, we are here taking the relatively conservative approach of that both photometric samples are of equal precision, which may lead to an overestimate of the SOGRAS random photometric errors. The solid (dashed) histograms in each panel are for the stars (galaxies). Each row corresponds to a given filter. Only fields with at least five bright sources were included in the histograms.

The mean photometric offsets for the stars are well centred around $\langle m - m_{\text{SDSS}} \rangle = 0$, with very few SOGRAS fields having $|\langle m -$

$m_{\text{SDSS}} \rangle| > 0.1$. The global median values of these offsets are 0.002, 0.006 and 0.005 for *g*, *r* and *i*, respectively. This result shows that our calibration was successful and consistent for the whole survey. The mean offset for galaxies is clearly larger and systematically positive. However, the typical galaxy systematics is still constrained to $\langle m - m_{\text{SDSS}} \rangle \leq 0.2$ in most cases. This larger systematics reflect the complexity of measuring galaxy fluxes and is likely caused by the differences in measuring methods applied to SOGRAS (MAG_AUTO) and SDSS (MODEL_MAG). Notice that the mean galaxy offset also tends to be larger in the *i* band, likely as the result of fringing residuals accumulated on galaxy angular scales.

The *rms* plots bear information on the random rather than systematic effects. Since they are also restricted to bright objects, we can estimate the photometric uncertainty in our calibration using the stellar *rms* of a typical field: $rms(g) \simeq 0.03$; $rms(r) \simeq 0.03$; $rms(i) \simeq 0.03$. For the galaxies, these typical values are larger, $rms(g) \simeq 0.11$; $rms(r) \simeq 0.09$; $rms(i) \simeq 0.13$, since they incorporate the effect of different magnitude definitions on top of that from calibration.

In Figs 6–8, we assess the SOGRAS random photometric errors, δ_m, as a function of S/N level. The values of δm (open points) are computed as the *rms* difference given in equation (1), but in this case, the sum is over all the galaxies in a given magnitude bin and the *rms* has been corrected for the systematic residual between SOGRAS and SDSS galaxy magnitudes in each field, whose distribution of values is shown as the darker histograms on the left-hand
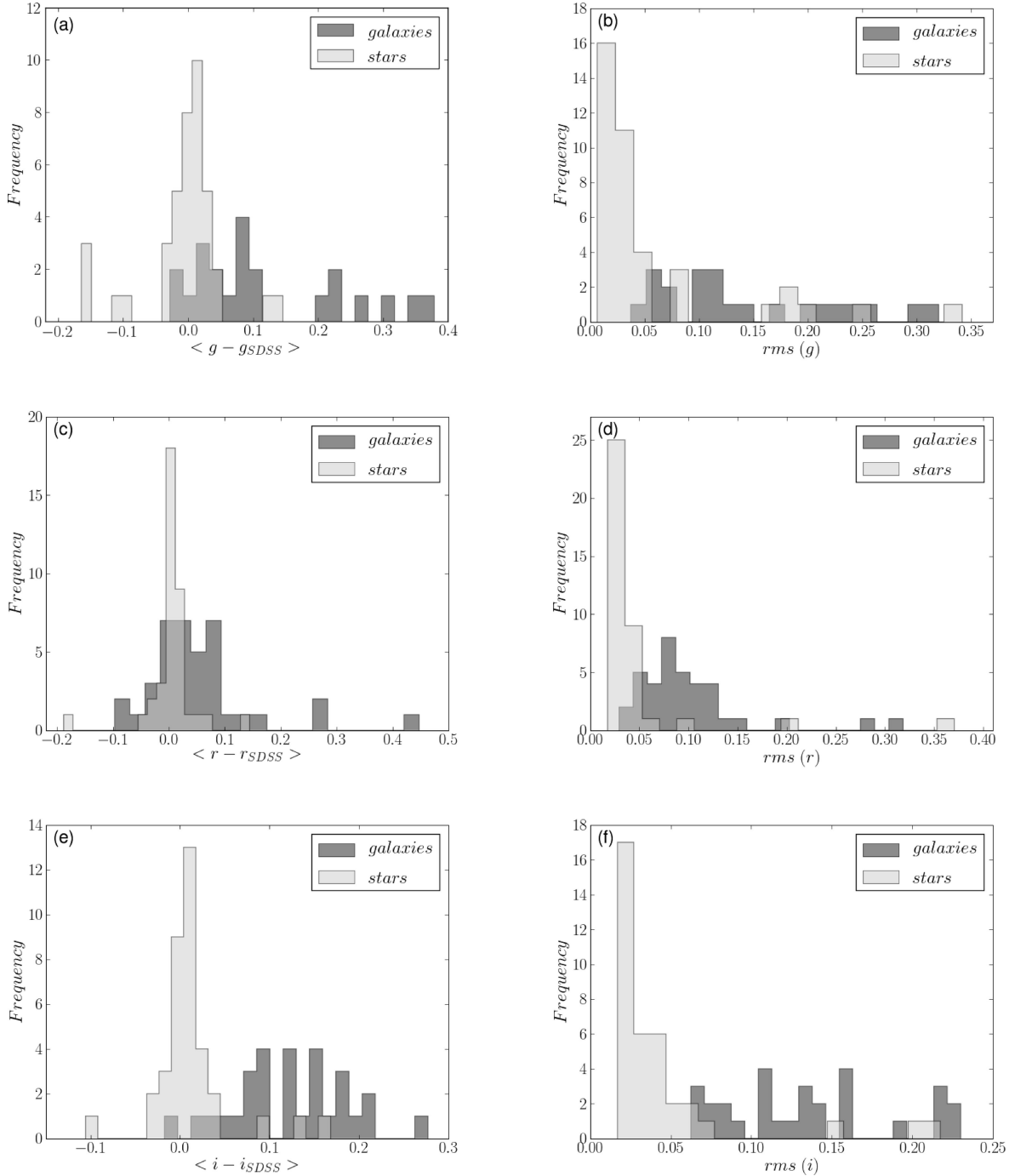
Figure 5. Panel (a): distribution of mean *g*-band magnitude differences between our photometry and that of SDSS for bright stars (solid) and galaxies (dashed). Panel (b): distribution of *rms* *g*-band magnitude differences between our photometry and that of SDSS for bright stars (solid) and galaxies (dashed). See equation (1) and text for details. Panels (c) and (d): same as in (a) and (b) but now for the *r* band. Panels (e) and (f): same as in (a) and (b) but now for the *i* band.

panels of Fig. 5. The uncertainties in δm are estimated via bootstrap resampling of all the galaxies in each magnitude bin. 1000 different realizations of the data were constructed using this method. We also plot the mean error in the MAG_AUTO values provided by SExtractor (MAGERR_AUTO) for the galaxies in each magnitude bin (filled points). The error bars in this case are the dispersion around the mean value.

The figures show a systematic increase in the photometric uncertainties as fainter galaxies are considered. The magnitude uncertainties based on the SExtractor errors are much smaller than the ones based on *rms* residuals relative to SDSS. This in part reflects our conservative assumption that both SOGRAS and SDSS are of equal accuracy. It may also reflect an underestimate of the photometric uncertainties by SExtractor. From these plots we infer that, on average, higher S/N are achieved in the *g*, than in the *r*, and than in the *i* bands. The detection limits for S/N > 3, which corresponds to $\delta_m > 0.36$, are found from the comparison with SDSS, being roughly $g \simeq 23.5$, $r \simeq 23$ and $i \simeq 22.5$.
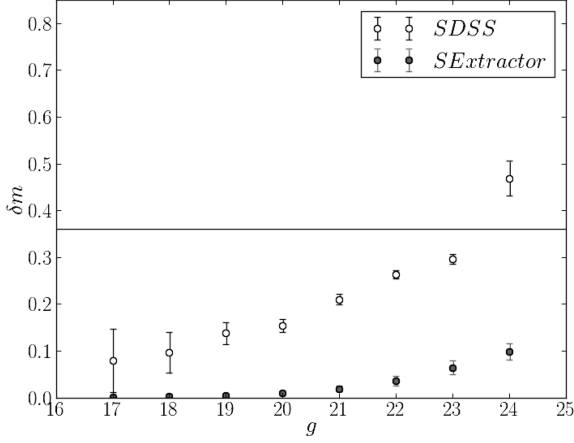
Figure 6. Magnitude uncertainties in *g* in each bin estimated as the *rms* residuals relative to SDSS divided by $\sqrt{2}$ (open points) and estimated as the mean value of the errors provided by SExtractor (MAGERR_AUTO, filled points). For the first case, the error bars were estimated using a bootstrap resampling technique, while for the second case, they correspond to the dispersion around the mean. The $\delta_m = 0.36$ line indicates the S/N = 3 level.
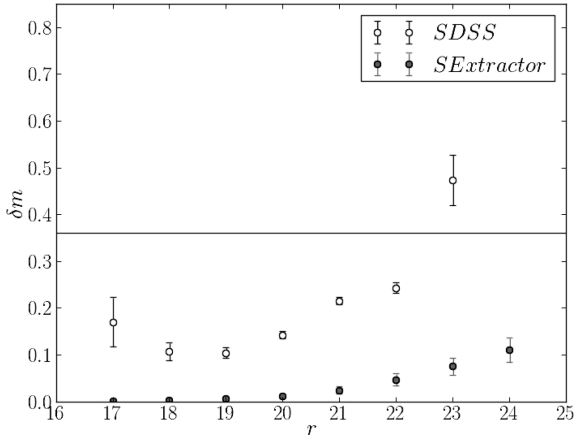

Figure 7. Same as Fig. 6, but for the *r* band.
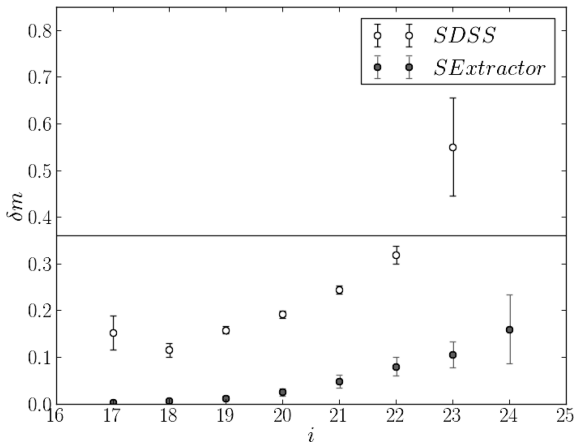
Figure 8. Same as Fig. 6, but for the *i* band.

4 GALAXY AND ARC CATALOGUES

4.1 Galaxy catalogues

We merged the catalogues resulting from the photometry (see Section 3.3) of the three bands in a final object catalogue, choosing the *i*-band catalogue as reference for object position. This means that we searched in the *g* and *r*-band catalogues for the objects that are in the *i* catalogue. Non-matched objects received a flag −99.99 in the corresponding filter. The final catalogue was saved as an FITS table and contains the information on position, magnitudes, morphological parameters and star–galaxy classification of the detected objects. In Table 2, we list the parameters in the final object catalogue and their corresponding definitions. This catalogue is publicly available upon request to the corresponding author.

In Fig. 9 we show colour–magnitude diagrams for two clusters, one at the low-*z* bin (SOGRAS0850+0015, $z = 0.20$, upper panels) and the other with higher *z* (SOGRAS0202−0055, $z = 0.50$, lower panels). In order to reduce contamination from field galaxies in these diagrams, galaxies that are located in a circular region of 100 arcsec (upper panels) and 60 arcsec (lower panels) around the cluster centres are shown with different symbols. Considering a flat ΛCDM model (with $\Omega_m = 0.3$, $\Omega_\Lambda = 0.7$ and $H_0 = 70$ km s^{-1} Mpc^{-1}) and the redshifts, these radii correspond to 0.33 Mpc and 0.4 Mpc, respectively. The red sequence is more visible in the lower *z* cluster, as expected. The colours of the red sequence also change slightly with *z*. The variation seems to be systematically larger for ($g - r$). For the relatively few high-*z* clusters where the red sequence is clearly visible, it tends to have bluer colours ($g - r \simeq 0.6$) than the low-*z* ones, for which ($g - r$) > 1. This is likely caused by the 4000Å Balmer break affecting the *g* filter at $z < 0.4$ but not the other passbands.

We chose to measure the morphology – semi-major (A) and semi-minor (B) axes and position angles derived from weighted second moments in SExtractor – in the *r* stacked images to optimize the combination of S/N and seeing. The seeing is not significantly

Table 2. Column labels in the SOGRAS object catalogue.

Parameter name	Definition
CLUSTER_ID	Cluster ID
OBJECT_ID	Object number
RA[a]	Right ascension (J2000)
DEC[a]	Declination (J2000)
X_IMAGE[a]	Object position along x
Y_IMAGE[a]	Object position along y
MAG_AUTO_G	Automatic aperture magnitude in the *g* band
MAGERR_AUTO_G	RMS error for AUTO magnitude in the *g* band
MAG_AUTO_R	Automatic aperture magnitude in the *r* band
MAGERR_AUTO_R	RMS error for AUTO magnitude in the *r* band
MAG_AUTO_I	Automatic aperture magnitude in the *i* band
MAGERR_AUTO_I	RMS error for AUTO magnitude in the *i* band
THETA_SKY[b]	Position angle (east of north)
ERRTHETA_SKY[b]	RMS error for position angle
A_IMAGE[b]	Semi-major axis for second moments
ERRA_IMAGE[b]	RMS error for semi-major axis
B_IMAGE[b]	Semi-minor axis for second moments
ERRB_IMAGE[b]	RMS error for semi-minor axis
ELLIPTICITY[b]	Ellipticity (1 – B_IMAGE/A_IMAGE)
CLASS_STAR[a]	Star–galaxy classification
FLAGS[a]	Extraction flags

[a]Measured in *i* band.
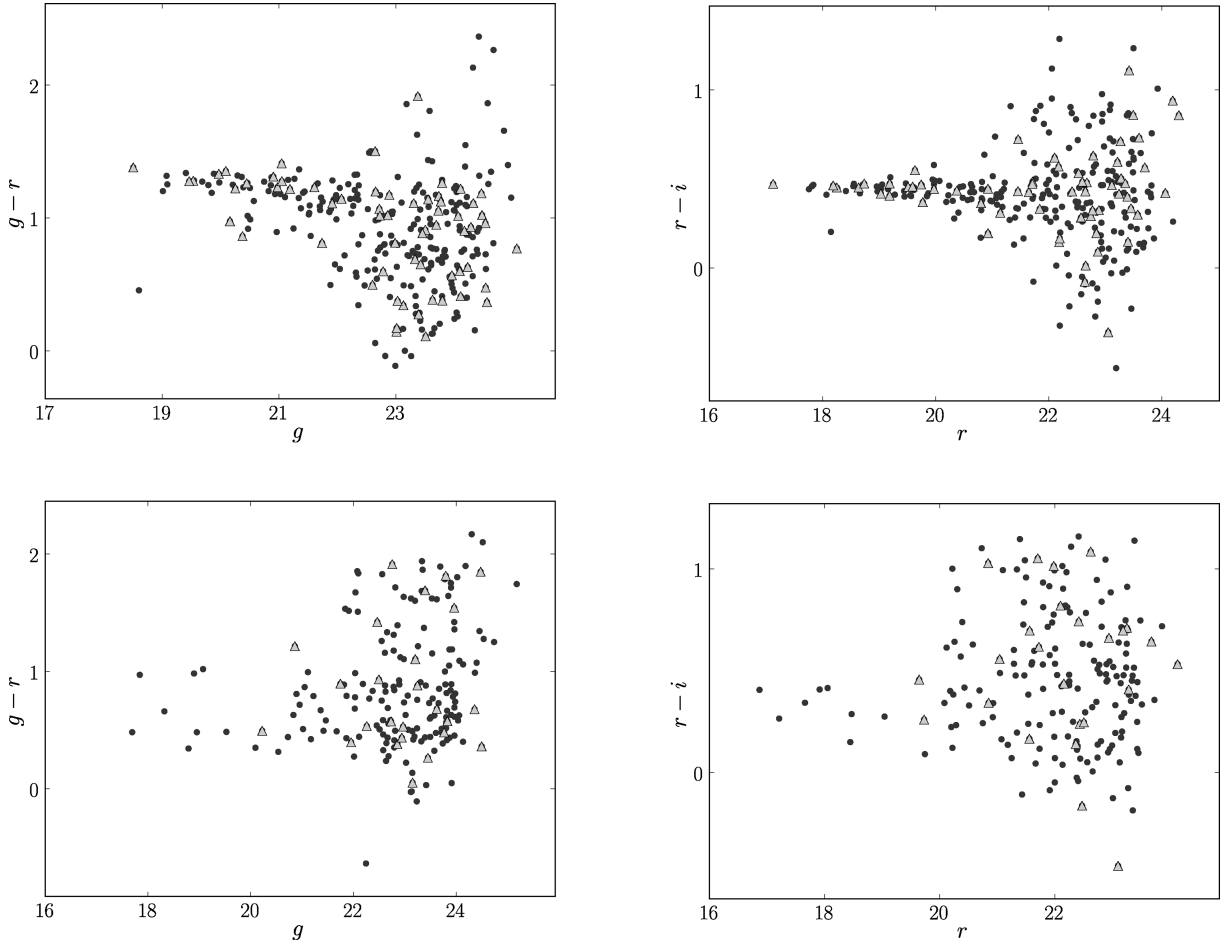[b]Measured in *r* band.

Figure 9. Colour–magnitude diagrams of clusters SOGRAS0850+0015 (upper panels) and SOGRAS0202−0055 (lower panels). $(g − r)$ colours are shown on the left-hand panels whereas $(r − i)$ colours are on the right-hand panels. The triangles indicate galaxies that are located in a circular region of 100 arcsec (upper panels) and 60 arcsec (lower panels) around the cluster centre. Considering a flat ΛCDM model (with $\Omega_m = 0.3$, $\Omega_\Lambda = 0.7$ and $H_0 = 70 \text{ km s}^{-1} \text{ Mpc}^{-1}$) and the redshifts, these radii correspond to 0.33Mpc and 0.4 Mpc, respectively.
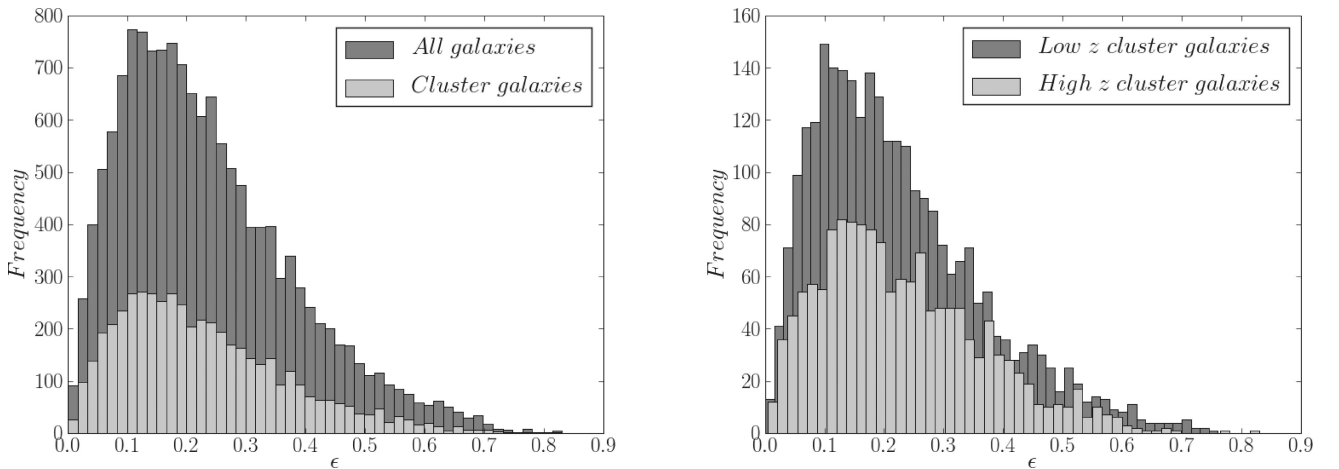
Figure 10. Left-hand panel: ellipticity distribution of all SOGRAS galaxies (all galaxies) and of SOGRAS galaxies which are located close to the clusters centre (cluster galaxies). Right-hand panel: ellipticity distribution of SOGRAS galaxies which are located close to the cluster centre for low- and high-z clusters. Galaxies were selected as objects with star–galaxy parameter CLASS_STAR < 0.85, as measured in r-band images.

degraded from the i to the r band (see Fig. 3), while the S/N increases from most objects (cf. Section 3.4). Therefore, the r band provides a balance between the higher S/N of the g band and the better seeing of the i band. Fig. 10 shows the distribution of the ellipticity $\epsilon =$

$1 − B/A$ of the SOGRAS galaxies. The left-hand panel shows the distribution of ϵ for all objects classified as galaxies and for all of them which are located close to the centre of the SOGRAS clusters (which we refer to as 'cluster galaxies'). The latter objects were

Table 3. Properties of the arc candidates identified in SOGRAS data. The photometric redshift z_{phot} of the clusters was taken from Table 1.

Cluster ID	z_{phot}	Arc ID	RA (J2000)	Dec. (J2000)	g	r	i	L (arcsec)	W (arcsec)	L/W
SOGRAS0321+0026	0.309	A	03:21:10.55	00:26:20.64	22.84	22.41	22.61	5.08	1.08	4.71
		B	03:21:12.76	00:26:23.73	24.13	23.63	22.90	1.23	0.62	2.00
SOGRAS0328+0044	0.322	A	03:28:15.79	00:44:49.59	22.73	20.72	20.25	5.93	3.03	1.95
		B	03:28:15.34	00:44:57.12	24.29	21.84	21.39	2.70	1.39	1.94
SOGRAS0014−0057	0.535	A	00:14:54.93	−00:57:02.44	21.84	21.21	20.65	12.24	1.31	9.34
SOGRAS0041−0043	0.564	A	00:41:09.22	−00:43:47.38	22.65	21.57	20.89	9.16	1.40	6.54
SOGRAS0940+0744	0.390	A	09:40:53.33	07:44:17.48	23.52	21.53	21.95	11.70	1.23	9.51
SOGRAS1023+0413	0.465	A	10:23:38.59	04:11:20.77	24.43	23.17	22.41	2.77	0.8 0	3.46
		B	10:23:41.45	04:10:41.62	24.36	23.19	22.57	2.93	1.10	2.66
		C	10:23:41.43	04:11:00.11	23.91	23.44	22.71	2.39	0.93	2.57

selected within circular regions around the cluster centres, whose angular radii were estimated visually. As in the case of Fig. 9, these cuts in angular separation were used just to reduce contamination from field galaxies.

Both distributions are peaked at $\epsilon \simeq 0.15$, and are strongly skewed towards higher values. The peak position is affected by the relatively large errors in ϵ for round objects, given the constraint that $\epsilon \geq 0$ always. Typical errors for round objects ($\epsilon \leq 0.15$) are of the order of $\sigma_\epsilon \simeq 0.07$. For more eccentric objects ($\epsilon > 0.15$), the errors are typical of $\sigma_\epsilon \simeq 0.04$. This behaviour is qualitatively confirmed by the analyses of early-type galaxies in nearby clusters (e.g. Fasano et al. 2010). In the right-hand panel we present the distribution of ϵ for SOGRAS galaxies that are located close to the clusters centre for low- and high-z clusters. The similarity between the distributions for low- and high-z clusters indicates that our shape determinations for high-z objects are not strongly degraded by atmospheric seeing and that shapes were properly measured for the galaxies in our catalogue.

4.2 New arc system candidates

We inspected all SOGRAS images in order to look for strong gravitational lens systems. We found six clusters (SOGRAS0321+0026, SOGRAS0328+0044, SOGRAS0014−0057, SOGRAS0041−0043,[11] SOGRAS0940+0744 and SOGRAS1023+0413) that show clear evidence of arcs and two clusters (SOGRAS0219+0022, SOGRAS0202−0055) that show probable arcs.

We identified 16 arc candidates close to the brightest members of eight cluster cores and most of them show bluer colours than the central cluster galaxies. Four of them are giant arcs and have length-to-width ratio (L/W) larger than 7. The remaining candidates are arclets, i.e. have smaller L/W. The length and width of the arc candidates were visually estimated, using the DS9 software.[12] The length was obtained by summing the two segments that connect the

extreme points to the arc geometric centre. The width corresponds to the distance between the arc 'borders' along the perpendicular bisector of the segment connecting the arc extrema passing through the arc centre.

The position, magnitude, length and width of the arc candidates in the six most probable strong lenses are displayed in Table 3. Contrary to the measurements of magnitude of other objects in the catalogue, which were obtained with SEXTRACTOR, the magnitudes of the arc candidates were measured using the task POLYPHOT from IRAF. This task computes the magnitudes inside polygonal apertures, providing more precise measurements of arc magnitudes, since it takes into account the arc shape. The polygons were visually defined and meant to incorporate the total flux of the arcs in each filter.

In Fig. 11 we show the candidate strong gravitational lens systems identified in SOGRAS data. Notice the systematically bluer colours of the arcs in comparison to that of a typical central cluster galaxy in our range of redshifts, $(g - r) \simeq 0.8$–1.0 (see Table 3 and online colour version of Fig. 11).

From the eight lens system candidates, two of them are in the low-z bin, four of them are in the high-z bin and the remaining two are in the extra sample. Concentrating on the six lensing systems from the low- and high-z samples, we infer that about 10 per cent of the clusters have arcs around them. This overall efficiency is in agreement with larger arc surveys, such as Gladders et al. (2003) and Hennawi et al. (2008). Despite the low number statistics, the results are also in qualitative agreement with the models in that they predict the high-z bin to have a larger efficiency in arc formation (e.g. Caminha et al., in preparation).

Follow-up observations of the first three lens systems candidates identified in SOGRAS images (in clusters SOGRAS0321+0026, SOGRAS0328+0044 and SOGRAS0219+0022) were conducted on the 8 m Gemini Telescope with the Gemini Multi-Object Spectrograph (Cypriano et al. 2010). The main aims of this follow-up programme were to confirm spectroscopically the gravitational lensing nature of these candidates, provide mass estimates for the clusters from the velocity dispersion of their member galaxies and perform strong lensing reconstruction of the projected mass distribution of the lenses. The results will be shown and discussed in a forthcoming paper.

Besides the multi-object spectroscopy, we obtained deep imaging to search for new arcs and to determine properties of the lensed galaxies (sources) such as their stellar populations and star formation rate. Visual inspection on these deeper images confirms

---

[11] This arc system was subsequently found by independent arc searches in CS82 data, both from a visual inspection of cluster images and from an automated arc search on the CS82 footprint (More et al., in preparation).
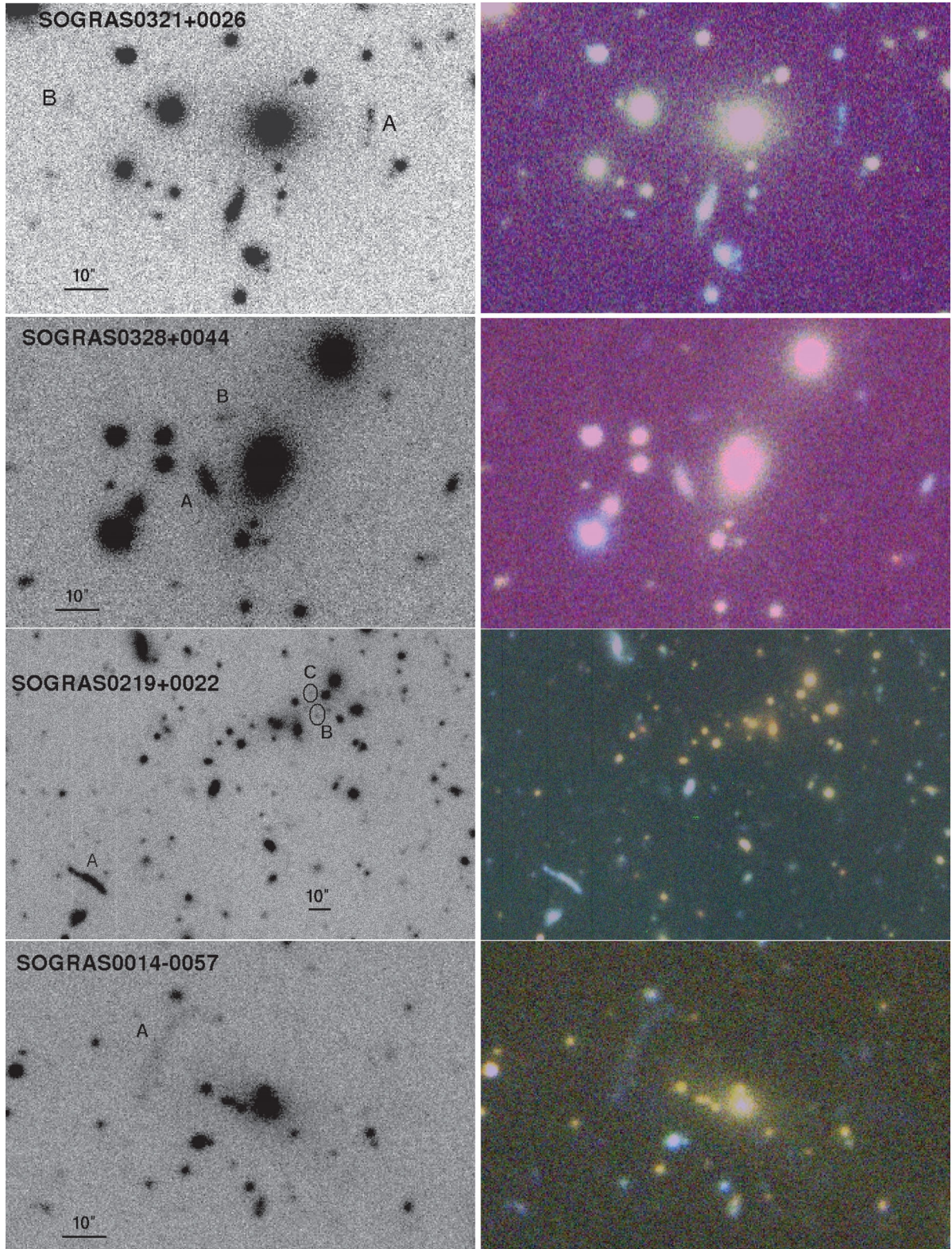[12] http://hea-www.harvard.edu/RD/ds9/

Figure 11. (Colour online) Strong lensing candidates identified in SOGRAS data. In all cases, the left-hand panel is the $g + r + i$ co-added image and the right-hand panel is the colour-composite image.

the arc candidates found in clusters SOGRAS0321+0026 and SOGRAS0328+0044, but revealed that the candidates of the cluster SOGRAS0219+0022 are unlikely to be arcs. The two of them which lie closer to the cluster are clearly seen as point sources in these images, while the third revealed itself as a superposition of two relatively edge-on galaxies. On the other hand, from a visual inspection of these images, several arc candidates are found in all of them, including in SOGRAS0219+0022.
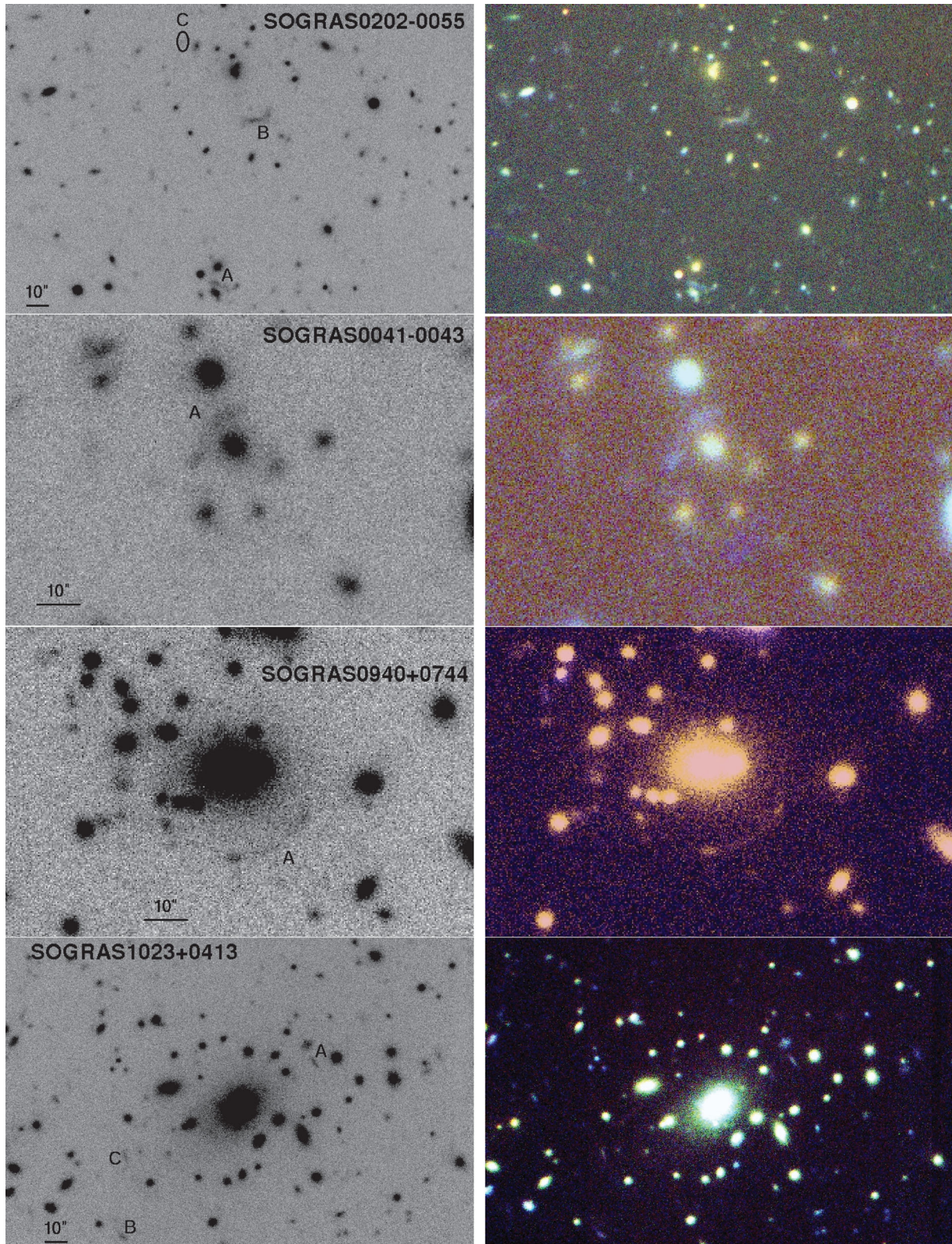
Figure 11 – *continued*

We thus conclude from our preliminary analysis of the deeper Gemini data that the number of lensing clusters has not been changed relative to our SOAR-based search, although some individual arc candidates have been added and some removed.

5 SUMMARY AND FUTURE PERSPECTIVES

We presented the first results from SOGRAS, an imaging survey towards 47 galaxy clusters using the SOAR telescope. We carefully

assessed the quality of our data products. We estimate our galaxy detection limits as $g \simeq 23.5$, $r \simeq 23$ and $i \simeq 22.5$ at S/N $\simeq 3$. Photometric calibration was performed using the SDSS stars in common with our fields with systematic uncertainties amounting to 0.002, 0.006 and 0.005 mag in g, r and i, respectively, and with essentially no systematics. Galaxy photometry suffered from a systematic offset typically of 0.04–0.12 mag in comparison to SDSS, likely caused by the different measurement methods used. Our source catalogue has over 19 000 entries, about 90 per cent of which are galaxies. We confirm that the data are of enough quality to allow a clear red sequence to be seen in most clusters in the low-z bin. Furthermore, seeing effects have not strongly affected shape measurements from our images, as attested by the fact that the distribution of axis ratios from our data closely resembles that for nearby cluster galaxies.

Although the number of targets in SOGRAS is smaller than in other arc surveys, the strength of our survey resides in the focus on two narrow redshift intervals whose differential lensing efficiency may yield direct information about the evolution of arc incidence. This works in a complementary way to previous studies of arcs around galaxy clusters, some of which have a larger overall statistics in the complete survey, but not in these redshift bins (e.g. Hennawi et al. 2008). The observations were carried out in similar conditions, with very good seeing, and with the same instrument, assuring a homogeneity of the data. Furthermore, our sample is unbiased, in the sense that there was no selection based on an a priori likelihood for an individual cluster to have arcs. These factors make the SOGRAS sample well suited for arc statistics studies, despite the relatively low number of objects.

Preliminary results from a visual inspection suggest an overall efficiency for arcs of about 10 per cent, consistent with previous studies (Gladders et al. 2003; Hennawi et al. 2008). A detailed study of arcs in SOGRAS, including comparison with model predictions, mass estimates from arcs, quantitative studies on arc morphology and arc detection will be presented in a separate paper.

Besides the strong lensing studies, this good image quality data can be used to perform a high S/N weak-lensing analysis by stacking the weak-lensing signal of all clusters in a given redshift bin to obtain an overall mass estimate for the clusters. We will also use the arcs and other strong lensing features to constrain the individual masses of the clusters (e.g. Cypriano et al. 2005). The data will also be used for detailed galaxy morphological studies using model-fitting methods, including the modelling of the PSF.

As far as we know, this is the first arc survey that specifically targeted optically selected clusters from the deep Stripe 82 *co-add*. This enabled us to select our low-z and high-z samples. Furthermore, this opens the possibility to exploit the combination with other surveys, by cross matching with the wealth of data in that region of the sky. In particular, most fields are in the CS82 region, which will provide complementary information around the clusters on larger scales.

This data set will also be used to validate and benchmark arc identification and characterization tools being developed by our group, including methods to enhance their detectability and arc finding algorithms. In some aspects, this small survey can be seen as a pathfinder for stage III photometric surveys such as DES, given that the SOAR images have similar depth as expected for those surveys.

SOGRAS can also be seen as a feasibility study for a unique arc survey profiting from the adaptive optics capabilities of SOAR in the optical and NIR, which can improve the PSF by a factor of 2 to 5.

REFERENCES

Abazajian K. N. et al., 2009, ApJS, 182, 543
Adelman-McCarthy J. K. et al., 2008, ApJS, 175, 297
Ahn C. P. et al., 2012, ApJS, 203, 21
Annis J. et al., 2005, preprint (astro-ph/0510195)
Annis J. et al., 2011, preprint (arXiv:1111.6619)
Bartelmann M., Huss A., Colberg J. M., Jenkins A., Pearce F. R., 1998, A&A, 330, 1
Bartelmann M., Meneghetti M., Perrotta F., Baccigalupi C., Moscardini L., 2003, A&A, 409, 449
Bayliss M. B., 2012, ApJ, 744, 156
Belokurov V., Evans N. W., Hewett P. C., Moiseev A., McMahon R. G., Sanchez S. F., King L. J., 2009, MNRAS, 392, 104
Bertin E., Arnouts S., 1996, A&AS, 117, 393
Blandford R. D., Narayan R., 1992, ARA&A, 30, 311
Boldrin M., Giocoli C., Meneghetti M., Moscardini L., 2012, MNRAS, 427, 3134
Cabanac R. A. et al., 2007, A&A, 461, 813
Coil A. et al., 2011, ApJ, 741, 8
Colless M. et al., 2001, MNRAS, 328, 1039
Cooray A. et al., 2010, preprint (arXiv:1007.3519)
Croom S. M. et al., 2009, MNRAS, 392, 19
Croom S. M., Smith R. J., Boyle B. J., Shanks T., Loaring N. S., Miller L., Lewis I. J., 2011, MNRAS, 322, L29
Cypriano E. S., Sodré L., Jr, Campusano L. E., Kneib J.-P., Giovanelli R., Haynes M. P., Dale D. A., Hardy E., 2001, AJ, 121, 10
Cypriano E. S., Lima Neto G. B., Sodré L., Jr, Kneib J.-P., Campusano L. E., 2005, ApJ, 630, 38

Cypriano E. S., Makler M., Santiago B., Furlanetto C., Lin H., Ferreira P., Hao J., Kubo J., 2010, Gemini program GS-2010B-Q-5

Dalal N., Holder G., Hennawi J. F., 2004, ApJ, 609, 50

Drinkwater M. J. et al., 2010, MNRAS, 401, 1429

Estrada J. et al., 2007, ApJ, 660, 1176

Fasano G. et al., 2010, MNRAS, 404, 1490

Furlanetto C. et al., 2013, A&A, 549, 80

Garilli B. et al., 2008, A&A, 486, 683

Gilbank D. G., Gladders M. D., Yee H. K. C., Hsieh B. C., 2011, AJ, 141, 94

Gladders M. D., Hoekstra H., Yee H. K. C., Hall P. B., Barrientos L. F., 2003, ApJ, 593, 48

Golse G., Kneib J.-P., Soucail G., 2002, A&A, 387, 788

Gonzalez A. H. et al., 2012, ApJ, 753, 163

Guzik J., Seljak U., 2002, MNRAS, 335, 311

Hao J. et al., 2010, ApJS, 191, 254

Hattori M., Kneib J., Makino N., 1999, Prog. Theor. Phys. Suppl., 133, 1

Hennawi J. F., Dalal N., Bode P., Ostriker J. P., 2007, ApJ, 654, 714

Hennawi J. F. et al., 2008, AJ, 135, 664

Hilbert S., Metcalf R. B., White S. D. M., 2007, MNRAS, 382, 1494

Hodge J. A., Becker R. H., White R. L., Richards G. T., Zeimann G. R., 2011, AJ, 142, 3

Horesh A., Ofek E. O., Maoz D., Bartelmann M., Meneghetti M., Rix H.-W., 2005, ApJ, 633, 768

Horesh A., Maoz D., Ebeling H., Seidel G., Bartelmann M., 2010, MNRAS, 406, 1318

Horesh A., Maoz D., Hilbert S., Bartelmann M., 2011, MNRAS, 418, 54

Ivezić Ž. et al., 2007, AJ, 134, 973

Johnston D. E., Sheldon E. S., Tasitsiomi A., Frieman J. A., Wechsler R. H., McKay T. A., 2007, ApJ, 656, 27

Jones D. H. et al., 2009, MNRAS, 399, 683

Kausch W., Schindler S., Erben T., Wambsganss J., Schwope A., 2010, A&A, 513, A8

Killedar M., Borgani S., Meneghetti M., Dolag K., Fabjan D., Tornatore L., 2012, MNRAS, 427, 533

Kneib J.-P., Natarajan P., 2012, A&AR, 19, 47

Kneib J.-P., Van Waerbeke L., Makler M., Leauthaud A., 2010, CFHT programs 10BF023, 10BC022, 10BB009

Kochanek C. S., Morgan N. D., Falco E. E., McLeod B. A., Winn J. N., Dembicky J., Ketzeback B., 2006, ApJ, 640, 47

Koester B. P. et al., 2007, ApJ, 660, 239

Kubo J. M. et al., 2010, ApJ, 724, L137

Lasker B. M. et al., 2008, AJ, 136, 735

Lawrence A. et al., 2007, MNRAS, 379, 1599

Li G. L., Mao S., Jing Y. P., Mo H. J., Gao L., Lin W. P., 2006, MNRAS, 372, L73

Luppino G. A., Gioia I. M., Hammer F., Le Fèvre O., Annis J. A., 1999, A&AS, 136, 117

Makler M., Cypriano E., Dúmet-Montoya H., Caminha B. G., Ferreira P., Estrada J., Lin H., 2008, SOAR program SO2008B-015

Makler M. et al., 2010, SOAR program SO2010B-023

Mandelbaum R., Seljak U., Cool R. J., Blanton M., Hirata C. M., Brinkmann J., 2006, MNRAS, 372, 758

Martin D. C. et al., 2005, ApJ, 619, L1

Meneghetti M., Dolag K., Tormen G., Bartelmann M., Moscardini L., Perrotta F., Baccigalupi C., 2004, Mod. Phys. Lett. A, 19, 1083

Meneghetti M., Fedeli C., Zitrin A., Bartelmann M., Broadhurst T., Gottlöber S., Moscardini L., Yepes G., 2011, A&A, 530, 17

More A., Cabanac R., More S., Alard C., Limousin M., Kneib J.-P., Gavazzi R., Motta V., 2012, ApJ, 749, 38

Newman J. A. et al., 2012, preprint (arXiv:1203.3192)

Oliver S. J. et al., 2012, MNRAS, 424, 1614

Papovich C. et al., 2011, Spitzer Proposal ID 80100

Redlich M., Bartelmann M., Waizmann J.-C., Fedeli C., 2012, A&A, 547, 66

Reis R. R. R. et al., 2012, ApJ, 747, 59

Richards G. et al., 2012, Spitzer Proposal ID 90045

Sand D. J., Treu T., Ellis R. S., Smith G. P., 2005, ApJ, 627, 32

Schechter P., 1976, ApJ, 203, 297

Sehgal N. et al., 2012, preprint (arXiv:1205.2369)

Sheldon E. S. et al., 2001, ApJ, 554, 881

Sheldon E. S. et al., 2004, AJ, 127, 2544

Smith G. P., Kneib J.-P., Smail I., Mazzotta P., Ebeling H., Czoske O., 2005, MNRAS, 359, 417

Thakar A. R., Szalay A. S., Fekete G., Gray J., 2008, Comput. Sci. Eng., 10, 30

The Dark Energy Survey Collaboration, 2005, preprint (astro-ph/0510346)

Tokovinin A., Cantarutti R., 2008, PASP, 120, 170

Tokovinin A., Cantarutti R., Tighe R., Schurter P., van der Bliek N., Martinez M., Mondaca E., 2010, PASP, 122, 1483

Treu T., 2010, ARA&A, 48, 87

Vuissoz C. et al., 2007, A&A, 464, 845

Wen Z.-L., Han J.-L., Jiang Y.-Y., 2011, Res. Astron. Astrophys., 11, 1185

Wiesner M. P. et al., 2012, ApJ, 761, 1

Zaritsky D., Gonzalez A. H., 2003, ApJ, 584, 691

Zieser B., Bartelmann M., 2012, preprint (arXiv:1204.0372)